

# Bursting and excitability in neuromorphic resonant tunneling diodes

Ignacio Ortega<sup>1,2</sup>, Oreste Piro<sup>1</sup>, Bruno Romeira<sup>3</sup>, and Julien Javaloyes<sup>1,2\*</sup>

<sup>1</sup> *Departament de Física, Universitat de les Illes Balears,*

*Cra. de Valldemossa, km 7.5, E-07122 Palma de Mallorca, Spain*

<sup>2</sup> *Institute of Applied Computing and Community Code (IAC-3),*

*Cra. de Valldemossa, km 7.5, E-07122 Palma de Mallorca, Spain and*

<sup>3</sup> *Ultrafast, Bio- and Nanophotonics, INL - International Iberian Nanotechnology Laboratory,*  
*Av. Mestre José Veiga s/n, 4715-330 Braga, Portugal*

(Dated: August 17, 2021)

We study in this paper the dynamics of quantum nanoelectronic resonant tunneling diodes (RTDs) as excitable neuromorphic spike generators. We disclose the mechanisms by which the RTD creates excitable all-or-nothing spikes and we identify a regime of bursting in which the RTD emits a random number of closely packed spikes. The control of the latter is paramount for applications in event-activated neuromorphic sensing and computing. Finally, we discuss a regime of multi-stability in which the RTD behaves as a memory. Our results can be extended to other devices exhibiting negative differential conductance.

Spike information processing and transmission in the form of events that occur at continuous times has numerous advantages over digital encoding and signaling. It is a key mechanism in the dynamics of neurons and the brain, which suggests its value in the development of biologically-inspired artificial intelligence. Neurons are *excitable systems*; they respond to an external stimulus by realizing a large amplitude response, typically in the millisecond and millivolt range, before returning to their rest state, provided that said stimulus is larger than a certain threshold. If this input is not sufficiently strong, a weak, exponentially decaying, response is obtained. For the duration of the response –known as lethargic time– the system is unable to respond to any other stimulus, irrespective of its amplitude [1–3]. The concept of excitability pervades many areas such as image processing [4], semiconductor structures [5] and lasers [6–8].

Several neuromorphic circuits have been proposed which attempt to emulate the transmission of information in the brain and the nervous systems, including the IBM TrueNorth chip [9] and the Intel Quark SE chip [10]. These approaches are still based on adapting the conventional CMOS architecture, and have some drawbacks, such as low frequency (kHz) and much higher power consumption than the brain. For low energy, sub-pJ/spike, synaptic-like functionalities, non-volatile materials such as resistive random-access memory, phase-change memory and spin-transfer torque magnetic random-access-memory offer alternatives to silicon, see [11] for a review. Despite remarkable progresses, fan-out and parasitic constraints of these approaches limit the power budget and frequency operation for scalable, high-speed solutions.

In this work, we provide a detailed analysis on the performance of quantum nanoelectronic resonant tunneling diodes (RTDs) as neuromorphic spike generators. Resonant tunneling diodes are promising candidates and are

the fastest electronic oscillators up to date, reaching frequencies in the order of the hundreds of GHz, with a world record of 1.98 THz [12, 13]. Their speed stems from the nanometric size ( $\sim 10$  nm) of the semiconductor active layer of the RTD in the epitaxial growth direction. This active layer consists of a double barrier quantum well (DBQW) nanostructure. This provides to RTD devices a current voltage with pronounced negative differential conductance which has been extensively applied for oscillator devices. Wang et al reported RTD oscillators with areas of 15 and 25  $\mu\text{m}^2$  operating at powers under 1 mW [14]. Asada's group reports a transmitter comprising a 1  $\mu\text{m}^2$  RTD with a maximum output power of 60  $\mu\text{W}$  [15, 16]. RTDs prospective applications as both transmitters and receivers of digital coding are being extensively investigated, as they can be modulated via either amplitude shift keying (ASK) or on-off keying (OOK). Recently, short-distance wireless data transmission at about 10 Gbps using RTD-based devices has been achieved [17, 18]. For neuron computation, early works evoked RTD-based devices as potential nanoelectronic candidates for cellular neural networks as a form of threshold logical gates [19].

The Hodgkin-Huxley, integrate and fire, or the Izhikevich models are widely used as test benches for neural spiking. They provide for different compromises between biological accuracy and computational cost. In comparison, Liénard oscillators [20] such as RTDs received comparatively less attention. The excitability of RTDs was disclosed in [21] both using electrical and optical stimuli, and optical spike regeneration coupling the RTD to laser diode and a time delayed feedback loop was demonstrated in [22]. Yet, a full theoretical characterization of the spiking and bursting dynamics of RTD devices is lacking. Importantly, the results presented here can be applied to other negative devices exhibiting differential conductance. Some recent examples include NDC devices using Van der Waals [23] or graphene/boron nitride [24] heterostructures.

\* julien.javaloyes@uib.es

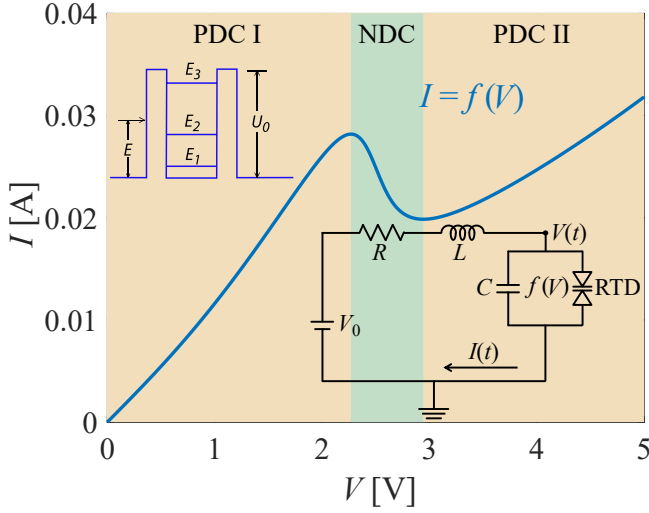


Figure 1. Current-voltage nonlinear relationship of the double barrier quantum well resonant tunneling diode. The regions with positive differential conductance (PDC I, PDC II) and negative differential conductance (NDC) are also illustrated. Upper inset: A symmetric double barrier quantum well nanosstructure where  $U_o$  is the potential barrier height, and  $E_1 - E_2$  are the resonant energy levels. Lower inset: Schematic circuit of the RTD oscillator.

The paper is organized as follows: In section I we recall the fundamentals of nanoelectronic RTD devices and the basic hypothesis underlying our modeling approach and the various types of solutions. In section II we give a detailed analysis of the excitable response of the RTD and discuss slow-fast dynamics and bursting. Finally, section III is devoted to the bifurcation analysis of our dynamical system, i.e., the qualitative changes of the system's responses as a function of its control parameters. We summarize our results in section IV.

## I. THEORETICAL MODEL

The active layer of nanoelectric RTD devices consists of a narrow bandgap semiconductor embedded between two thin layers of wide bandgap semiconductors, thus forming a double barrier quantum well (DBQW) nanostructure (figure 1, upper inset). Depending on the voltage applied across the device, the Fermi level of the incident electrons may resonate with the confinement levels of the quantum well, thus locally maximizing their probability to cross it (i.e., maximum probability corresponds to a local peak of current). As a result, the current-voltage characteristic of the RTD is a nonlinear function with one or more regions of negative differential conductance in between regions of positive differential conductance [18],

$$f(V) = a \ln \left( \frac{1 + e^{\frac{q}{k_B T}(b-c+n_1 V)}}{1 + e^{\frac{q}{k_B T}(b-c-n_1 V)}} \right) \times \left( \frac{\pi}{2} + \tan^{-1} \left( \frac{c - n_1 V}{d} \right) \right) + h \left( e^{\frac{q}{k_B T} n_2 V} - 1 \right). \quad (1)$$

The expression 1 is derived by applying the Fermi-Dirac statistics to a double barrier quantum well.  $T$  is the temperature,  $q$  is the electron charge and  $k_B$  is the Boltzmann's constant. The inner parameters  $a$ ,  $b$ ,  $c$ ,  $d$ ,  $n_1$ ,  $n_2$  and  $h$  depend on the geometry of the barrier and its resonant energy levels, although they can also be determined by fitting experimental data [25]. In this article, the inner parameters have the following values:  $a = 0.0039$  A,  $b = 0.05$  V,  $c = 0.0874$  V,  $d = 0.0073$  V,  $n_1 = 0.0352$ ,  $n_2 = 0.0031$ ,  $h = 0.0367$  A,  $T = 300$  K. These parameters produce an I-V characteristic typical of III-V semiconductor RTD devices (e.g. InGaAs/ALAs materials) and with micrometric overall device size. A plot of the function  $f(V)$  with these values is shown in figure 1. This characteristic is referred to as N-shaped since it has a region of negative slope (or conductance) embedded between two regions of positive conductance. We will refer to these regions as NDC, PDC I and PDC II.

A system of two first-order differential equations for the current and voltage was proposed in [20], accounting for the dynamics of a double barrier quantum well resonant tunneling diode (DBQW RTD) connected to a DC voltage input. A schematics of the circuit is shown in figure 1, lower inset. The dynamics equations are derived from Kirchhoff laws,

$$\mu \dot{V} = I - f(V), \quad (2)$$

$$\mu^{-1} \dot{I} = V_0 - V - RI. \quad (3)$$

Here,  $V(t)$  is the voltage across the RTD and  $I(t)$  is the total current.  $V_0$  is the bias DC voltage,  $R$  is the circuit intrinsic resistance and the parameter  $\mu$  is defined as  $\mu = \sqrt{\frac{C}{L}}$ , where  $L$  and  $C$  are the equivalent inductance and capacitance, respectively, which sets the circuit's natural frequency. This parameter reduction has been achieved by defining a dimensionless time  $t = \omega_0 \tilde{t}$ , setting  $\dot{X} \equiv dX/dt$  and where  $\omega_0 = \frac{1}{\sqrt{LC}}$  is the RTD natural frequency. We note that Eqs. (2,3) represents a Liénard oscillator [20, 26, 27].

After proper normalization, there are only three parameters, which depend on the circuit design: the resistance  $R$ , the stiffness parameter  $\mu$  and the bias  $V_0$ . As discussed in section II A, sufficiently small values of  $\mu$  are necessary for the RTD to exhibit excitability. Depending on the parameters  $R$ ,  $\mu$  and  $V_0$ , the system given by Eqs. (2,3) may exhibit fixed points and periodic solutions, as well as a coexistence between two or more

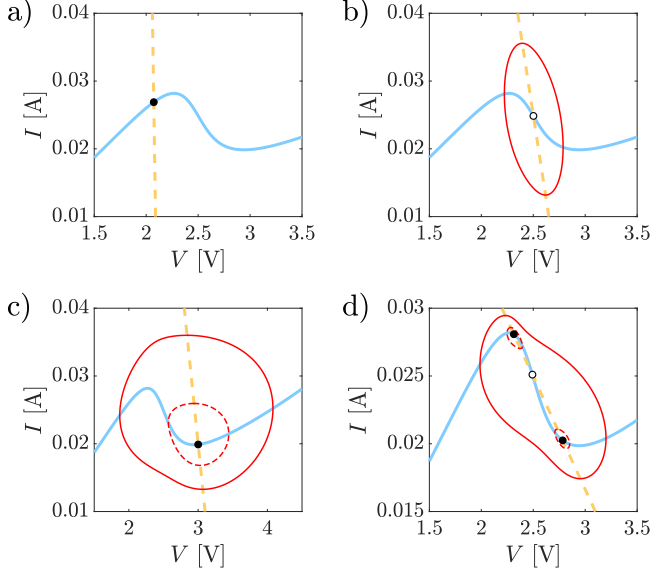


Figure 2. Stable and unstable solutions in equilibrium of equations (2,3) under different parameters. The blue and yellow lines correspond to the conditions  $\dot{V} = 0$  and  $\dot{I} = 0$ , respectively. The intersections correspond to fixed points. Stable (resp. unstable) periodic orbits are depicted in continuous (resp. dotted) red lines: a)  $R = 1 \Omega$ ,  $\mu = 0.04 \Omega^{-1}$ ,  $V_0 = 2.1 \text{ V}$ . b)  $R = 10 \Omega$ ,  $\mu = 0.04 \Omega^{-1}$ ,  $V_0 = 2.75 \text{ V}$ . c)  $R = 10 \Omega$ ,  $\mu = 0.01 \Omega^{-1}$ ,  $V_0 = 3.2 \text{ V}$ . d)  $R = 60 \Omega$ ,  $\mu = 0.01 \Omega^{-1}$ ,  $V_0 = 3.998 \text{ V}$ .

equilibrium solutions. Some examples of coexisting solutions for different choices of parameters are illustrated in figure 2.

**Fixed point:** The system exhibits an equilibrium point wherever the nullclines intersect (figure 2). In other words, the following equations must be satisfied:

$$f(V) - I = 0, \quad (4)$$

$$V + RI - V_0 = 0, \quad (5)$$

which implies solving the nonlinear equation  $V + Rf(V) = V_0$ . The stability of a fixed point is given by the eigenvalues of the Jacobian of (2,3) that reads

$$J = \begin{bmatrix} -\frac{1}{\mu}f'(V) & \frac{1}{\mu} \\ -\mu & -\mu R \end{bmatrix}. \quad (6)$$

We have

$$\lambda_{\pm} = -\frac{1}{2} \left( \frac{f'(V)}{\mu} + \mu R \right) \pm \frac{1}{2} \sqrt{\left( \frac{f'(V)}{\mu} - \mu R \right)^2 - 4}. \quad (7)$$

The fixed point is stable if the trace is negative and the determinant, positive. For this system, the aforementioned inequalities read,

$$f'(V) > -\mu^2 R, \quad (8)$$

$$f'(V) > -\frac{1}{R}. \quad (9)$$

When they are saturated, these two inequalities correspond to the locus bistability via Saddle-Node bifurcations and to the creating of limit cycles via Andronov-Hopf bifurcations, respectively. It is clear from these inequalities that being either in the PDC I or the PDC II region is a sufficient (although not necessary) condition for a fixed point to be stable since  $f'(V) > 0$ . The number of steady states is determined to a great extent by whether the resistance  $R$  is larger than a critical value, given by the absolute value of the reciprocal of the minimal conductance,

$$R_C = -\frac{1}{\min \{f'(V) : V \in \mathbb{R}\}}. \quad (10)$$

If  $R \leq R_C$ , the system has a unique fixed point for all values of  $\mu$  and  $V_0$ . If  $R > R_C$  the system has between one and three fixed points, as the load line may intersect the I-V characteristic in up to three points. This is geometrically intuitive but it will also be discussed in part III. For the typical parameter set used in our analysis, the critical resistance is  $R_C \simeq 38.484 \Omega$ .

**Periodic solution:** The system (2,3) may also exhibit one or more periodic solutions which may be stable or unstable. The stability of a periodic solution is given by the Floquet multipliers [26]. A limit cycle may arise from a stable focus as the latter becomes stable, in an supercritical Andronov-Hopf (AH) bifurcation [1, 26]. Figure 2b Shows a stable limit cycle surrounding an unstable fixed point. Simulations of equations (2,3) also show a stable limit cycle in coexistence with a stable fixed point as well as an unstable limit cycle in between (figure 2c). This suggests the existence of a subcritical AH bifurcation. As mention above, a circuit with high resistance ( $R > R_C$ ) may exhibit multiple fixed points and, with them, multiple limit cycles. A particular case of this is depicted in figure 2d.

## II. EXCITABILITY IN AN RTD CIRCUIT

### A. Slow-fast dynamics

As mentioned in part I, the parameter  $\mu$  is referred to as the stiffness coefficient and it is of key importance because it determines whether or not the circuit is suitable for spike generation. If  $\mu \sim 1$ , the periodic solutions are well-rounded orbits, with the coordinates  $V(t), I(t)$  evolving over time in quite smooth fashion, as shown in the example in figure 3a,c and Fig. 2. However, as  $\mu$  is decreased, the orbits become stiffer. If  $\mu$  is sufficiently small (several times smaller than  $1/R_C$ ), four stages can be recognized in each period; two slow stages and two fast stages, as it is the case with the periodic solution shown in figure 3b,d. In the first slow stage, the orbit overlaps the N-shaped RTD current-voltage characteristic in the PDC I, and  $V(t)$  and  $I(t)$  increase steadily.

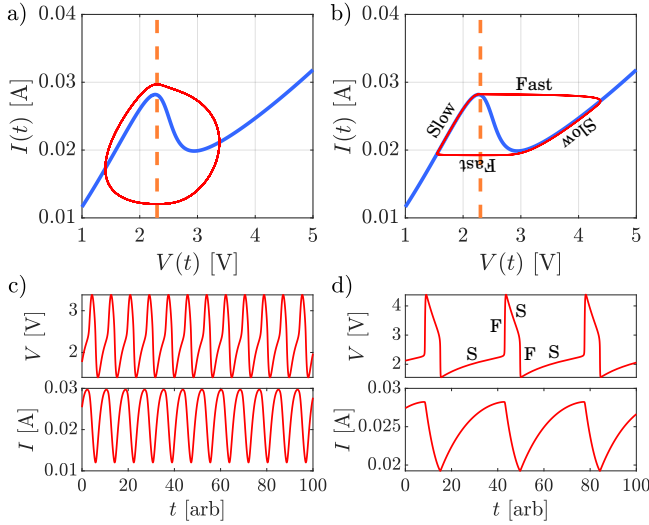


Figure 3. Periodic solution on the phase space for  $R = 0.01 \Omega$ ,  $V_0 = 2.3 \text{ V}$ , and two different values for the stiffness coefficient: *a*)  $\mu = 0.008 \Omega^{-1}$ , *b*)  $\mu = 0.001 \Omega^{-1}$ . The I-V curve (blue line) and load line (dashed orange line) are included. *b, c*) Evolution of over time of the output variables  $V$  and  $I$  corresponding to the periodic solutions in panels *a* and *b*, respectively. The system exhibits stages of slow and fast dynamics when  $\mu$  is small enough.

This means that  $I \approx f(V)$ , i.e., all the incident electrons are crossing the double barrier quantum well. When the local maximum of the I-V characteristic is reached, the first fast stage initiates, and the voltage suddenly rises. This happens because far from the I-V curve, if  $\mu$  is very small then any change in  $V$  is significantly larger than the corresponding change in  $I$ , which remains constant and larger than  $f(V)$ . This means that not all incident electrons are crossing the barrier, and charges accumulate at the ends. The orbit reaches the I-V curve at the PDC II in a very short time, and the second slow stage starts;  $V(t)$  and  $I(t)$  decrease steadily as they follow the  $\dot{V} = 0$  nullcline until reaching its local minimal point. The second fast stage begins with a sudden voltage decrease and almost no change in current. Since  $I < f(V)$  in this stage, the ends of the DBQW is discharged. The ends of the DBQW being charged and discharged are schematically represented in figure 1 (inset) by the intrinsic capacitance  $C$ . The slow and fast stages can be easily distinguished in each period of the profile of  $V(t)$  and they give it the characteristic of a periodic spike signal. The variable  $I(t)$  on the other hand, does not have a sudden rise or drop, thus being an overall slow variable.

Because of the two stages of slow dynamics the period of the limit cycle increases as the stiffness coefficient  $\mu$  decreases. Once time normalization is removed one can appreciate that the period is proportional to  $L$ , see Eq. (6) in [21]. The exact limit cycle period depends on the parasitic capacitance and inductance the device is fabricated with. As a reference, Wang et al report the fab-

rication of an RTD with a DBQW of about 7 nm width, a mesa area of  $16 \mu\text{m}^2$  and a parasitic capacitance as low as about  $C = 78 \text{ fF}$  [18]. Together with a transmission line inductance of  $L \sim 100 \text{ nH}$ , a stiffness coefficient of  $\mu = \sqrt{\frac{C}{L}} \approx 0.001 \Omega^{-1}$  can be achieved. Under this setting, a normalized refractory time in the order of  $T \sim 10$  like in Fig. (3b) would translate into a frequency in the order of the GHz. This value is two orders of magnitude lower than the frequencies typically reported for RTDs with similar dimensions [12, 14, 17]. It is because these devices are fabricated to operate as oscillators in smooth dynamics with higher values of  $\mu$ .

## B. Excitable response

Let us consider a configuration in the circuit where the load line intersects the RTD I-V curve in a unique point either in the PDC I or II but close to the NDC (i.e., close to either the local maximum or minimum). In this situation, the intersection point is a stable attractor. Figure 4 shows several responses of the system after perturbations from its stable point of equilibrium. Indeed, if the perturbation is above a certain threshold ( $\Delta I \simeq 0.0282 \text{ A}$  here), the system exhibits a single orbit, thus producing a spike. The orbit is reminiscent of the stable limit cycle obtained for slightly different values of the bias when the RTD is biased in the NDR. On the other hand, the response to a weak perturbation is a small response that decays exponentially.

## C. Spikes and bursts

Adding noise into the system biased either in the first or second PDC region is a way to perturb it in a permanent, random manner. For instance, an electrical noise input can be incorporated in the model as an additive white noise function  $\xi(t)$  in equation 2. Here, the stochastic process  $\xi(t)$  satisfies  $\langle \xi(t) \rangle = 0$  and  $\langle \xi(t)\xi(t') \rangle = \eta^2 \delta(t' - t)$ . Some of these perturbations might be stronger than the excitability threshold and will therefore trigger a spike. The higher the noise intensity  $\eta$ , the more likely an above-threshold perturbation is to occur and hence the more frequent the spikes are expected to be, with the possibility to achieve coherence resonance behavior [28], as no interval between consecutive spikes can be shorter than the refractory time. Figure 5a,b shows the system's response biased in the first PDC region, under the same parameters ( $R, \mu, V_0$ ) and different levels of noise. As expected, spikes are triggered more frequently as the noise intensity is increased. Because of the strongly asymmetric character of the I-V curve, there is a substantial qualitative difference between the spikes generated with the circuit biased at the first and the second PDC region, as in the latter case, the spikes tend to arise in bursts,

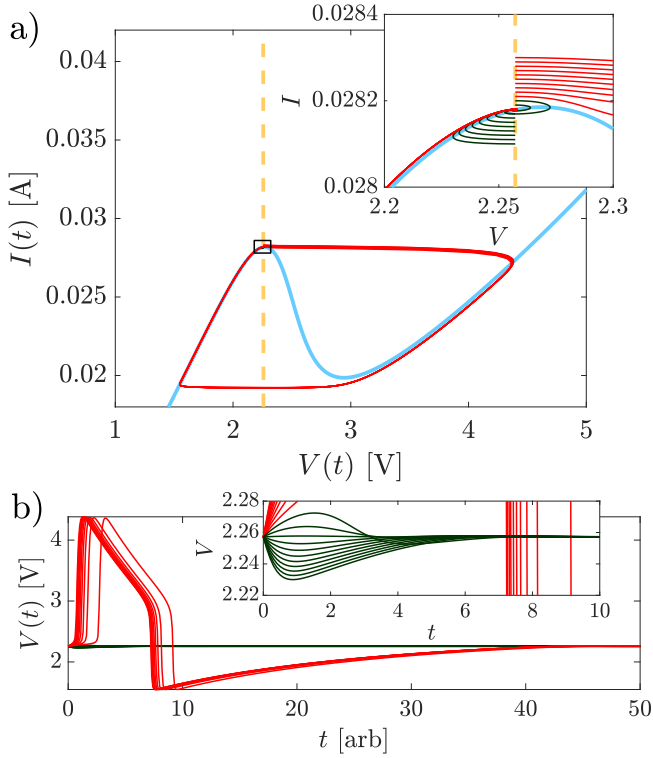


Figure 4. System's response to several perturbations out of its natural equilibrium for parameters  $R = 0.1 \Omega$ ,  $\mu = 0.001 \Omega^{-1}$ ,  $V_0 = 2.26 \text{ V}$ . *a)* Trajectories on the phase plane ( $V, I$ ). *b)* Evolution of variables  $V$  and  $I$  over time. Current perturbations under  $0.0282 \text{ A}$  induce an exponential decay (green curves and insets). Perturbations above this threshold lead to the generation of a single spike before returning to the attractor (red curves).

separated by the refractory time, as shown in figure 5*c* and in agreement with the results of [21].

### III. BIFURCATION ANALYSIS

We analyze in this section the response of the system (i.e., stable and unstable solutions in equilibrium) in terms of the free parameters  $R$ ,  $\mu$  and  $V_0$ . In particular, we are interested in understanding which parameter combination leads to an effective single-event excitable spike generator versus a bursting generator. Two cases will be discussed separately, depending on whether the intrinsic resistance  $R$  is under or over the critical value  $R_C$ . If  $R < R_C$  (section III A), the nullclines intersect in a unique point and therefore, the regions defined by the equilibrium responses and the bifurcations that separate them are rather simple to describe. Indeed, the geometry of these regions is not substantially affected by the value of the resistance. The fixed point may change stability via an AH bifurcation, which also gives rise to a limit cycle. The limit cycle is stable or unstable depending on

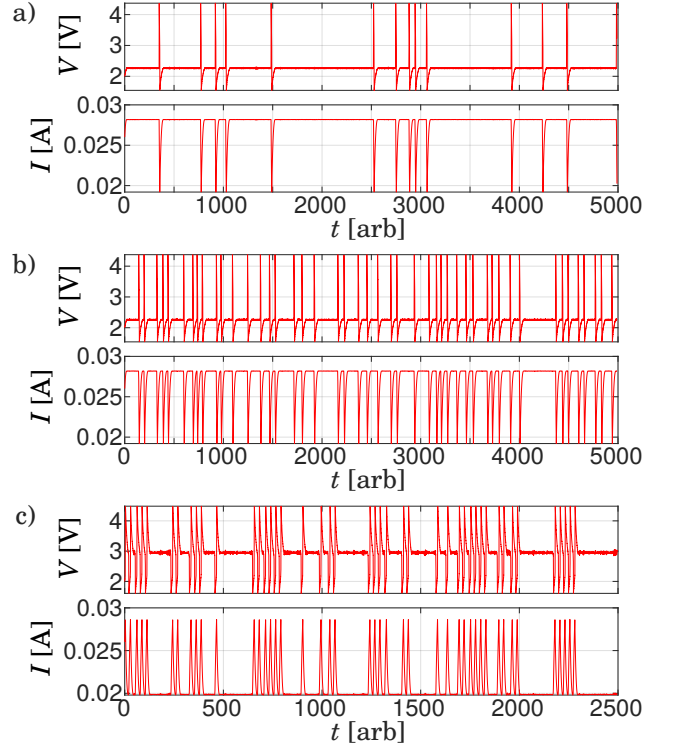


Figure 5. Numerical traces of output pulses randomly generated by perturbing with additive white noise at  $R = 0.01 \Omega$  and  $\mu = 0.001 \Omega^{-1}$ . The system is biased in the first PDC region in panels *a* and *b* and in the second PDC region in panel *c*. The input bias voltage and input noise intensity are: *a)*  $V_0 = 2.26 \text{ V}$ ,  $\eta = 0.009 \text{ V}$ , *a)*  $V_0 = 2.26 \text{ V}$ ,  $\eta = 0.011 \text{ V}$ , *a)*  $V_0 = 2.94 \text{ V}$ ,  $\eta = 0.014 \text{ V}$ .

whether the bifurcation is supercritical or subcritical. In the latter case, the unstable limit cycle becomes stable via a fold bifurcation. On the other hand, if  $R > R_C$  (section III B), there may be up to three fixed points, which may arise or vanish via a saddle-node bifurcation. This opens the possibility of limit cycles surrounding one fixed point or all of them, as well as the possibility of a limit cycle colliding a saddle point in a homoclinic bifurcation. All this makes the range of responses and transitions more rich and complex to describe in this case.

The branches of periodic and homoclinic solutions as well as the bifurcations relating to those have been computed by using DDE-BifTool [29] package (version 3.1.1). The fixed point branches and AH bifurcations have been computed analytically through curve parametrization. The saddle-node bifurcations have been evaluated numerically.



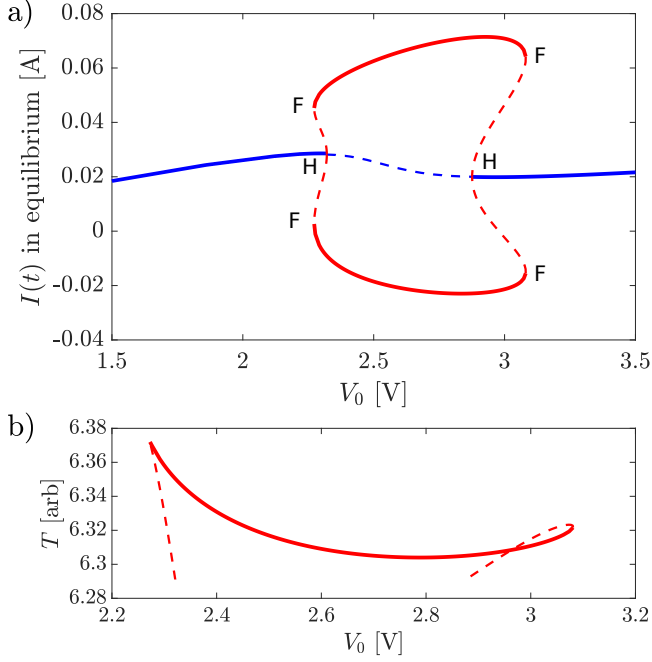


Figure 6. *a)* Bifurcation diagram illustrating the  $I$ -coordinate of the fixed point (in blue) and the  $I$ -maximum and minimum of the limit cycle (in red) versus the input bias voltage  $V_0$  for  $R = 1 \Omega$  and  $\mu = 0.05 \Omega^{-1}$ . Solid lines represent stable solutions and dashed lines represent unstable solutions. AH bifurcations (H) and limit cycle folds (F) are also shown. *b)* Evolution of the period  $T$  of the limit cycle along the branch.

### A. Case $R < R_C$

#### 1. Fixed point and limit cycle branches

The goal in this section is to trace the evolution of the equilibrium solutions in terms of the input bias voltage  $V_0$  while the parameters  $R$  and  $\mu$  are fixed. As discussed in part I, calculation of the fixed point requires in principle solving the system of equations (4,5), which cannot be done analytically given the complexity of the function  $f(V)$ . However, a branch of fixed points can be characterized as a parametric curve; instead of tracking the evolution of the fixed point (namely, its coordinates  $V$  and  $I$ ) in terms of  $V_0$ , Eqs. (4,5) may be re-written as,

$$V_0 = V + RI, \quad (11)$$

$$I = f(V), \quad (12)$$

thus expressing  $V_0$  and  $I$  in terms of  $V$ , which serves as the free parameter. This allows to continue the branch without the need to solve any equations; neither analytically nor numerically. This method was used to compute all the fixed point branches presented in this work. The

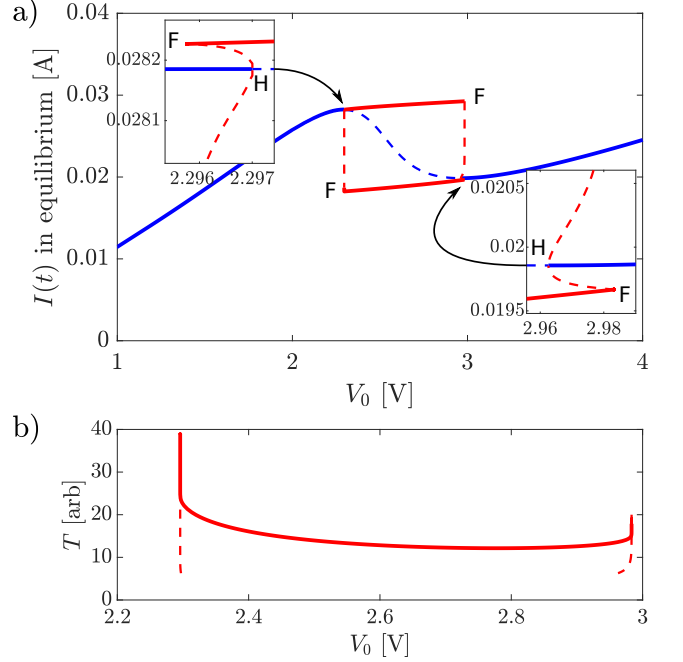


Figure 7. *a)* Bifurcation diagram illustrating the  $I$ -coordinate of the fixed point (in blue) and the  $I$ -maximum and minimum of the limit cycle (in red) versus the input bias voltage  $V_0$  for  $R = 1 \Omega$  and  $\mu = 0.002 \Omega^{-1}$ . Solid lines represent stable solutions and dashed lines represent unstable solutions. The insets show a zooming in the proximity each AH bifurcation (H). The limit cycle folds (F) are also shown. *b)* Evolution of the period  $T$  of the limit cycle along the branch.

parametric curve  $(V_0(V), I(V))$  is plotted in figures 6(a) and 7(a) for  $R = 1 \Omega$  and two different values of  $\mu$ .

Note how the fixed point parametrization does not depend on  $\mu$ . The stability, however, does; The fixed points are unstable when either  $f'(V) < -\mu^2 R$  or  $f'(V) < -1/R$ . The latter cannot happen since  $R < R_C$  (i.e.,  $f'(V) > -1/R$  always) but the former can. In fact, under the assumption that  $f(V)$  is monotonous in the NDC region, its derivative is then a basin-shaped function with a unique minimal value  $f'_{\text{MIN}} = -1/R_C < 0$ . Thus, provided that  $\mu^2 < 1/(RR_C)$ , the equation  $f'(V) = -\mu^2 R$  has exactly two solutions. Let us call these solutions  $V^{(1)}$  and  $V^{(2)}$ . The fixed point is unstable if the input bias voltage is between the values  $V_0^{(1,2)} = V^{(1,2)} + Rf(V^{(1,2)})$  and it is stable elsewhere. These transitions are candidates of AH bifurcations. Indeed, substitution of  $f'(V) = -\mu^2 R$  in equation 7 leads to,  $\lambda_{\pm} = \pm i\sqrt{1 - (\mu R)^2}$ , which is a purely imaginary number (provided that  $R < R_C$  and  $\mu^2 < 1/(RR_C)$ , then  $(\mu R)^2 < 1$ ). On the other hand, if  $\mu^2 \geq 1/(RR_C)$ , the fixed point is stable regardless of  $V_0$ .

The limit cycle branches were computed with DDE-BifTool. For sufficiently large values of  $\mu$ , the periodic branch arises subcritically from the fixed point at  $V_0^L = 2.231 \text{ V}$  and  $V_0^R = 2.876 \text{ V}$ , see Figure 6(a) ob-

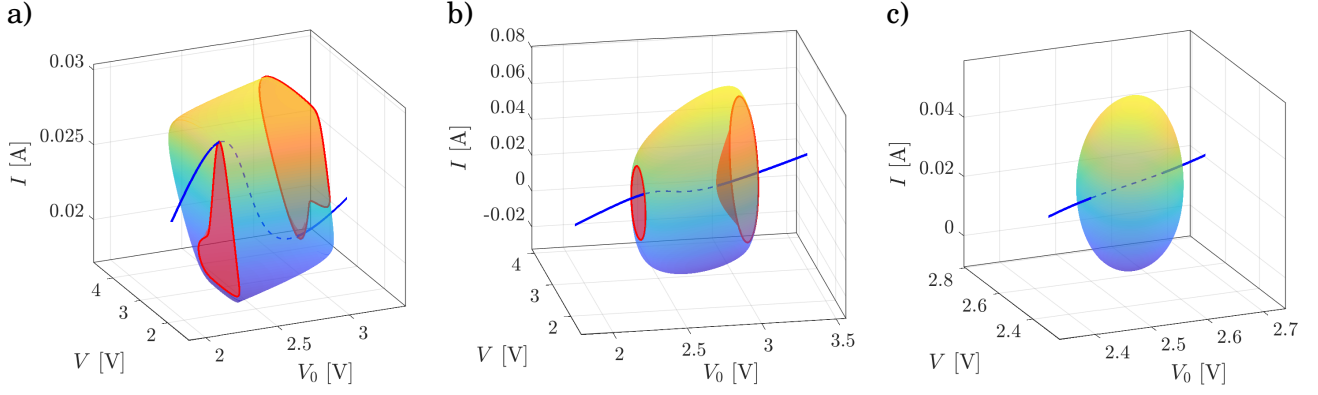


Figure 8. Three-dimensional bifurcation diagram illustrating the stable and unstable steady state branches, solid and dashed blue lines, respectively, the stable limit cycle branch (colored gradient surface), the unstable limit cycle branch (red surface) and limit cycle fold (red curves) versus the input bias voltage  $V_0$  for  $R = 1 \Omega$  and different values of  $\mu$ : a)  $\mu = 0.002 \Omega^{-1}$ , b)  $\mu = 0.05 \Omega^{-1}$ , c)  $\mu = 0.14 \Omega^{-1}$ .

tained with  $R = 1 \Omega$  and  $\mu = 0.05 \Omega^{-1}$ . For this relatively large value of  $\mu$ , the dynamics is smooth and so are the solution branches. There are two ranges of input bias where the stable fixed point and the stable limit cycle coexist. These ranges have a width of about 0.05 V at the left side and 0.2 V at the right side. Figure 6(b) shows the limit cycle period in terms of  $V_0$ . The period is locally maximized at the proximity of both fold bifurcations and it has a plateau in the stable part of the branch, at about  $V_0 = 2.8$  V. The solutions along this branch have a smooth, (quasi) sinusoidal profile.

Figure 7(a) illustrates the bifurcation diagram for the same value of  $R = 1 \Omega$ , but a much smaller stiffness coefficient  $\mu = 0.002 \Omega^{-1}$  allowing for slow-fast dynamics. While the AH bifurcation points are essentially not displaced ( $V_0^L = 2.297$  V and  $V_0^R = 2.961$  V), the branch of periodic solutions changes dramatically; in the proximity of the AH bifurcation points, the amplitude of the limit cycle increases explosively. A zooming in both regions show that the bifurcations are still sub-critical, whilst the ranges of bistability are much more narrow (in the order of 0.001 V at the left side and 0.01 V at the right side). On both sides, the unstable limit cycle folds and becomes stable. Solutions along the stable part of the branch are very similar to those in figure 3(b), with stages of low and fast dynamics that can be clearly distinguished, and their amplitude and shape do not change substantially with  $V_0$ . Figure 7(b) shows the period along the branch. The results are qualitatively similar to those in figure 6(b); the period is maximal at the proximity of the AH bifurcations with a plateau in between, where the limit cycle is stable, although the increasing of the period towards the maximal values is very sharp. There is an important quantitative difference, however, as the period is one order of magnitude larger than that computed for  $\mu = 0.05 \Omega^{-1}$ .

The bifurcation diagrams from figures 7(a) and 6(a) are

shown again in perspective in figure 8 (panels a and b, respectively), where both coordinates  $V$  and  $I$  of the equilibrium solutions are plotted versus the parameter  $V_0$ . A new bifurcation diagram is included where  $\mu = 0.14 \Omega^{-1}$  (panel c). We already know that for  $\mu = 0.002 \Omega^{-1}$ , the dynamics is stiff, the limit cycle folds are sharp and the bistability ranges are very narrow. As  $\mu$  is increased, the limit cycle branch becomes smoother and the bistability ranges widen, particularly the right one, which is always wider than the left one. For values of  $\mu$  above  $0.05 \Omega^{-1}$  however, this tendency has reversed, and the bistability ranges become narrow again, until they eventually vanish. At  $\mu = 0.14 \Omega^{-1}$ , the AH bifurcations have become supercritical and there is no unstable periodic solutions nor periodic solution folds (panel c). In regards to the AH points, they become closer as  $\mu$  increases and they eventually coalesce at  $\mu < 1/\sqrt{RR_C} \approx 0.1703 \Omega^{-1}$ . Consequently, the periodic solutions also vanish.

## 2. Evolution of the bifurcations in the space of parameters

In this section, the AH bifurcation and limit cycle fold branches are characterized as curves in the  $(V_0, \mu)$  plane while  $R$  is fixed at different values under  $R_C$ . The AH points satisfy the equation  $f'(V) = -\mu^2 R$ . This, along with equations 4 and 5 are used to parametrize the AH branch in terms of  $V$ ,

$$V_0 = V + Rf(V), \quad (13)$$

$$\mu = \sqrt{-\frac{f'(V)}{R}}, \quad (14)$$

where  $V$  is in the NDC region (so  $\mu(V) \in \mathbb{R}$ ). The latter reaffirms that AH bifurcations can only occur in the

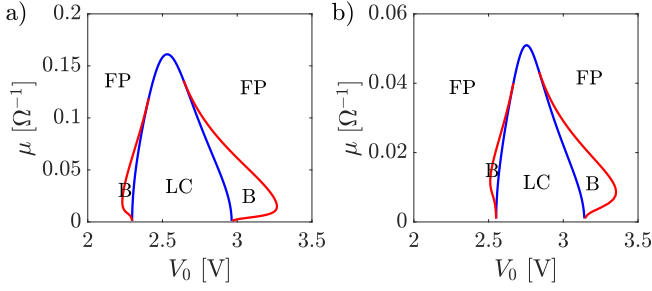


Figure 9. Andronov-Hopf bifurcation branches (blue line) and limit cycle fold branches (red line) on the  $(V_0, \mu)$  plane for  $R = 1 \Omega$  (a) and  $R = 10 \Omega$  (b). There is a unique stable fixed point (FP) outside the region delimited by the AH branch which is unstable inside. In this region, there is a stable limit cycle (LC). In the regions between the AH branch and the limit cycle fold branch, the system is bistable (B) in the sense that the stable fixed point and the stable limit cycle coexist.

NDC region. Figure 9 show the AH branch for different resistances under  $R_C$ . In general, the branch defines a uniquely evaluated, hill-shaped function of  $\mu$  versus  $V_0$ . The maximal value of  $\mu$  at the top of the branch is  $\mu_{\text{MAX}} = 1/\sqrt{RR_C}$ , where the left and right AH points collide. Above this point, there is no unstable fixed points nor limit cycles at all.

The limit cycle fold branches were numerically computed with DDE-BifTool and they are also included in figure 9. As  $\mu$  approaches zero, the fold branches approach the ends of the AH branch asymptotically. As  $\mu$  increases, the fold points move away from the AH branch and the bistability ranges (coexistence of an attractor with a stable limit cycle) broaden, until they reach a plateau and the fold branches approach the AH branch tangentially until they collide with it close to the top. Consequently, the AH bifurcation transitions from sub-critical to super-critical. In general, the bistability range at the right of the AH branch is broader than the one at the left. This will be discussed in more detail in section III C.

The above analysis is consistent with figures 6, 7 and 8, and it is valid for all positive resistances under  $R_C$  as the branches retain their geometric characteristics. On the quantitative basis, however, the branches shift rightward and become smaller with increasing  $R$ , as  $\mu_{\text{MAX}}$  decreases with the inverse of the square root of the resistance.

## B. Case $R > R_C$

### 1. Fixed point and limit cycle branches

If  $R > R_C$  the system may exhibit up to three fixed points since the nullclines may now have more than one intersection, which depends specifically on the position coefficient of the load line, i.e., the input bias voltage  $V_0$ .

Consequently, the fixed point branch is not uniquely evaluated in terms of  $V_0$  but it folds backwards and then forwards again, as illustrated in figure 10. In this regime the RTD may behave as a memory [30]. The folds occur when the load line intersects the current-voltage characteristic tangentially and induce saddle-node bifurcations. This can be corroborated by computing the eigenvalues at the folds; Tangential intersection implies  $f'(V) = -1/R$ . Substitution of the latter in equation 7 reduces the eigenvalues to  $\lambda_+ = 0$  and  $\lambda_- = \frac{1}{\mu R} - \mu R$  at both folds. If  $\mu < 1/R$ , the first eigenvalue is positive, suggesting that as the fixed point crosses the saddle-node bifurcation, one eigenvalue remains positive while the other changes sign, thus transitioning from an unstable node to a saddle point. All the latter implies that the fixed point transitions from an unstable focus to an unstable node somewhere in between the AH bifurcation and the saddle-node. The process is reversed as we move along the branch; the saddle point becomes an unstable node again, then an unstable focus and finally, a stable focus at the second AH bifurcation. All these transitions are shown in figure 10, panels a and b. As  $\mu$  approaches  $1/R$ , the transitions become closer and coalesce at each fold. On the other hand, if  $\mu > 1/R$ , the non-zero eigenvalue is negative; as the fixed point passes along the fixed point branch (and thus, the saddle-nodes), it transitions from a stable node to a saddle point and then back into a stable node (figure 10, panel c). Thus, there is no AH bifurcation when  $\mu > 1/R$ . From all the above it is concluded that, whenever the system exhibits three fixed equilibrium points, the middle one is always a saddle. Finally, by using the parametric form of the fixed point branch (eqs (11,12)), we find that the bias voltages for which the saddle-nodes occur are  $V_0 = V_{\text{SN1}} + Rf(V_{\text{SN1}})$  and  $V_0 = V_{\text{SN2}} + Rf(V_{\text{SN2}})$ , where  $V_{\text{SN1}}$  and  $V_{\text{SN2}}$  are the solutions of  $f'(V) = -1/R$ .

The existence of a saddle fixed point in the system allows for the possibility of a limit cycle colliding with it and thus becoming a homoclinic curve, which separates the limit cycle branch into two or more branches. A tiny separation can be appreciated in figure 10(a). From the upper AH bifurcation,  $V_0 \approx 3.98 \text{ V}$ , an unstable limit cycle arises, which surrounds the upper attractor. The branch continues until the lower part of the limit cycle coalesces with the saddle point and becomes a homoclinic curve, at about  $V_0 \approx 3.96 \text{ V}$ . At a slightly smaller input bias, a new unstable limit cycle arises from a homoclinic curve that surrounds all the fixed points. This limit cycle branch then folds, becomes stable and extends until  $V_0 \approx 4.196 \text{ V}$ , where it folds again and becomes unstable. The unstable limit cycle collides with the fixed point in the lower AH bifurcation at  $V_0 \approx 4.062 \text{ V}$ . As  $\mu$  increases (while  $R$  is kept fixed), the right fold of the limit cycle branch approaches -and enters- the range defined by the saddle-nodes. Consequently, the right unstable limit cycle branch collides with the saddle fixed point branch, which produces two new homoclinic curves, as shown in figure 10.b. As  $\mu$  is further increased, the limit cy-



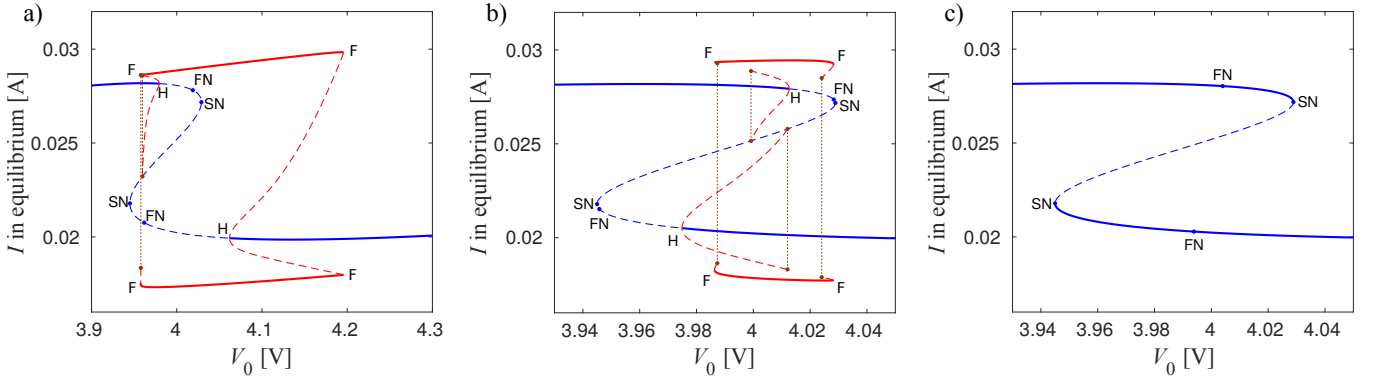


Figure 10. Bifurcation diagram illustrating the  $I$ -coordinate of the fixed point (blue lines) as well as the  $I$ -maximum and minimum of the limit cycle (red lines) and homoclinic curves (brown dots) versus the input bias voltage  $V_0$  for  $R = 60 \Omega$  and different values of  $\mu$ : a)  $\mu = 0.006 \Omega^{-1}$ , b)  $\mu = 0.0115 \Omega^{-1}$ , c)  $\mu = 0.03 \Omega^{-1}$ . Solid lines represent stable solutions and dashed lines represent unstable solutions. Andronov-Hopf bifurcations (H), limit cycle folds (F), saddle-node bifurcations (SN) and focus-node transitions (FN) are also illustrated. As  $\mu$  increases, the AH bifurcations and focus-node transitions approach the saddle-node bifurcation, and a second pair of homoclinic curves arise. For  $\mu > 1/R$ , there is no AH bifurcation and no periodic nor homoclinic solutions.

cles and homoclinic curves vanish (figure 10.c) by mechanisms that will be explained in section III B 2.

Figure 11 shows the bifurcation diagrams from 10, panels a and b, in perspective, including both coordinates  $V$  and  $I$ . The two homoclinic curves in the middle surround the upper attractor and the lower attractor, respectively. These homoclinics are illustrated in figure 12, panels a and b. We refer to these curves as type-1 homoclinic and type-2 homoclinic. The remaining two outer homoclinics surround all three fixed points as illustrated in figure 12, panels c and d. We refer to these curves as type-3 homoclinic and type-4 homoclinic, respectively.

## 2. Evolution of the bifurcations in the space of parameters

Figure 13 illustrates the bifurcation branches as curves in the  $(V_0, \mu)$  plane, for a fixed parameter  $R = 60 \Omega$ . The two saddle-node bifurcations define two parallel, vertical branches since, as already discussed in section III B 1, their positions in the bifurcation diagram do not depend on  $\mu$  and are given by  $V_0 = V_{SN1} + Rf(V_{SN1})$  and  $V_0 = V_{SN2} + Rf(V_{SN2})$ , where  $f'(V_{SN1}) = f'(V_{SN2}) = -1/R$ . For  $R = 60 \Omega$ , the positions of the saddle-nodes are estimated at  $V_0 \approx 4.029 \text{ V}$  and  $V_0 \approx 3.945 \text{ V}$ . It was also discussed in section III B 1 that, above  $\mu = 1/R$ , the saddle-nodes correspond to transitions from a stable node to a saddle, while below  $\mu = 1/R$ , they correspond to transitions from an unstable node to a saddle. This is represented in figure 13 as solid and dashed green lines, respectively.

Figure 13 also shows that when  $R > R_C$ , there is not one AH bifurcation branch but two of them. This happens because, since the fixed point branch is not a uniquely evaluated curve, the upper and lower AH bifurcations do

not coalesce with one another but switch sides instead, at  $\mu \approx 0.0095 \Omega^{-1}$  (this can be appreciated in figure 10.b, where the upper AH point is now at the right side and the lower AH point, at the left side). As  $\mu$  is further increased, the lower and upper AH branches approach the left and right saddle-nodes, respectively, and they eventually coalesce at  $\mu = 1/R \approx 0.0167$ .

From the analytical point of view, the parametric form of the AH bifurcation branch given by Eqs (13,14) is still valid. However, an additional restriction applies when  $R > R_C$ . The eigenvalues at the AH points were computed as  $\lambda_{\pm} = \pm i\sqrt{1 - (\mu R)^2}$ , which are meant to be purely imaginary; thus,  $\mu < 1/R$ . Substitution of parametric equation 14 in the latter inequality leads to  $f'(V) > 1/R$ . This restriction, together with the restriction  $f'(V) < 0$  required by equation 14, imply that the curve parameter  $V$  must be in the NDC region, but not in the interval  $[V_{SN1}, V_{SN2}]$ . In conclusion, the AH branch being split into two results from a discontinuity in the domain of the parametric form.

The limit cycle fold and homoclinic branches were continued with DDE-BifTool. The branches are illustrated in figure 13. When  $R > R_C$ , there is a single limit cycle fold branch instead of two. This happens because the homoclinic bifurcations disconnect the stable part of the limit cycle branch and thus the folds do not coalesce with the AH points. Instead, the folds become closer as  $\mu$  increases until they coalesce at the top of the fold branch at  $\mu \approx 0.0123 \Omega^{-1}$ . Above this point, there is no stable limit cycles anymore. The type-1 and type-3 homoclinic branches arise at  $\mu \approx 0.0111 \Omega^{-1}$ , as the left unstable limit cycle branch coalesces with the saddle point branch in the proximity to the left saddle-node. On the other hand, the type-2 and type-4 homoclinic branches arise at the bottom of the  $(V_0, \mu)$  plane, together with the

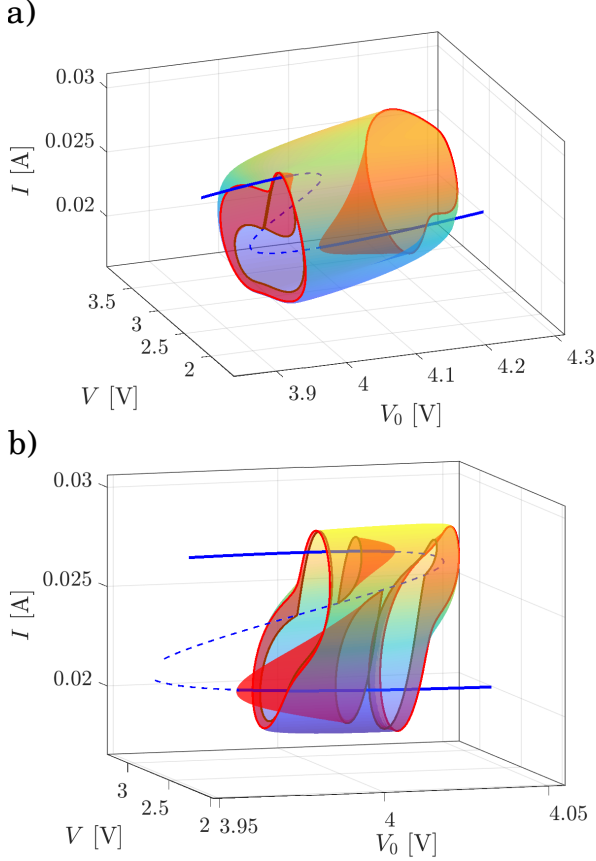


Figure 11. Three-dimensional bifurcation diagram illustrating the stable point branch (solid blue line), unstable point branch (dashed blue line), stable limit cycle branch (color gradient surface), unstable limit cycle branch (red surface), limit cycle fold (red curves) and homoclinic solutions (brown curves) versus the input bias voltage  $V_0$  for  $R = 60 \Omega$  and different values of  $\mu$ : a)  $\mu = 0.006 \Omega^{-1}$ , b)  $\mu = 0.0115 \Omega^{-1}$ .

upper AH and left limit cycle fold branches. The type-3 and type-4 homoclinic branches remain close to each side of the limit cycle fold branch. At  $\mu \approx 0.012 \Omega^{-1}$ , they fold down and at  $\mu \approx 0.0118 \Omega^{-1}$ , they coalesce with the type-1 and type-2 homoclinics and with each other. The type-3 and type-4 homoclinics vanish, while the type-1 and type-2 homoclinics simply switch sides, as they involve opposite eigendirections of the saddle point. At  $\mu = 1/R \approx 0.0167$ , the type-1 homoclinic branch coalesce with the upper AH branch and with the right saddle-node branch. This triple coalescence is known as a Bogdanov-Takens (BT) bifurcation and has codimension 2 [1]. Also at  $\mu = 1/R$ , the type-2 homoclinic branch coalesce with the lower AH branch and the left saddle-node branch in another BT bifurcation.

The description of the stable solutions becomes more complex when  $R > R_C$ , as there may be now two stable fixed points in addition to the stable limit cycle, which in turns allows more multistabilities. These multistabilities

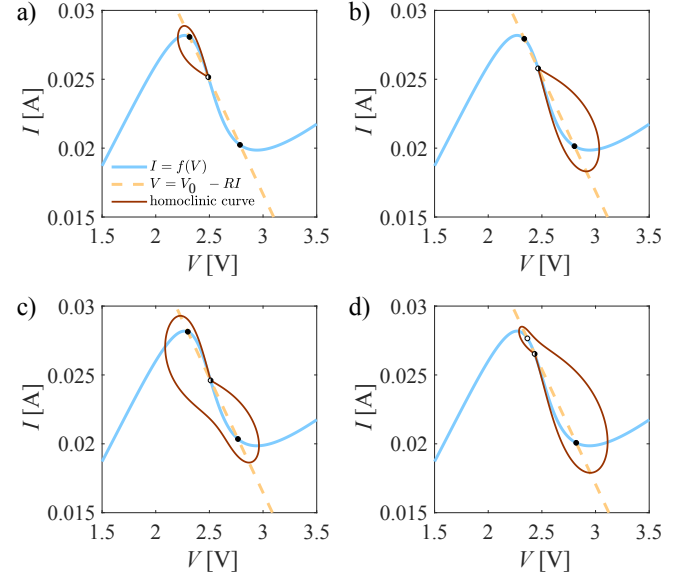


Figure 12. Homoclinic curves shown in figures 10.b and 11.b, arising for parameters  $R = 60 \Omega$ ,  $\mu = 0.0115 \Omega^{-1}$  and different values of  $V_0$ : a) Type-1 homoclinic,  $V_0 = 3.999 \text{ V}$ . b) Type-2 homoclinic,  $V_0 = 4.012 \text{ V}$ . c) Type-3 homoclinic,  $V_0 = 3.987 \text{ V}$ . d) Type-4 Homoclinic,  $V_0 = 4.024 \text{ V}$ .

are summarized Fig 14, which only includes the bifurcation branches beyond which the stable solutions vanish or become unstable, i.e, the AH bifurcations, the limit cycle fold and the saddle-node bifurcations above  $\mu > 1/R$ . The saddle-node and AH branches limit the upper attractor the the left side of the figure, the lower saddle-node and AH branches limit the lower attractor to the right side, and the limit cycle fold limit the stable limit cycle inside of it. These regions intersect and produce bistabilities as well as a small region at the center of the figure where the three stable solutions coexist.

### C. Suitable parameters for spike generation

In regards to the interest in utilizing the RTD circuit theoretically represented by equations (2,3) as an excitable spike generator, it has already been discussed that the stiffness parameter  $\mu$  needs to be small (no bigger than  $\sim 0.002 \Omega^{-1}$ ) for the stable limit cycle to produce spikes. As discussed in section II B, the input bias voltage  $V_0$  needs to be tuned in such a way either the upper or the lower fixed point is stable, but in the proximity of the region where there is a stable limit cycle. For the parameters of the nonlinear function  $f(V)$  chosen in this work and resistances of  $R = 10 \Omega$  or smaller, the value of  $V_0$  to achieve this is around 2.3 V if the circuit is biased in the first PDC region and around 3 V is the circuit is biased in the second PDC region. For a higher resistance such as  $R = 60 \Omega$ , these values have to be increased to around 3.95 V and 4.15 V, respectively. The bias in

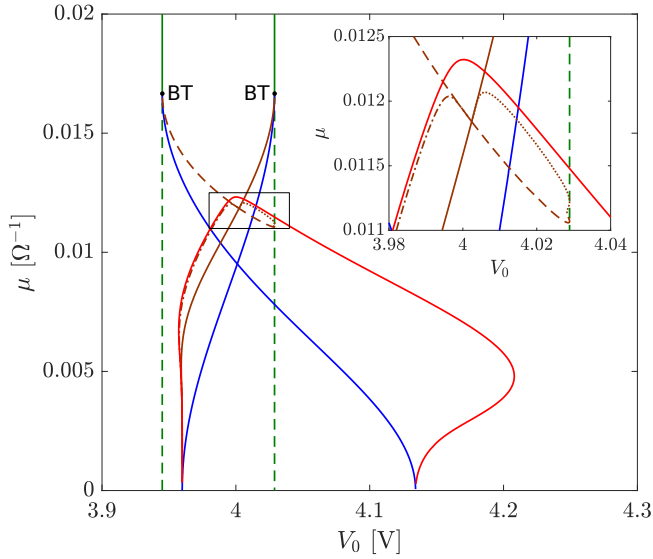


Figure 13. Bifurcation branches represented as curves on the  $(V_0, \mu)$  plane for  $R = 60 \Omega$ : Andronov-Hopf bifurcations (blue line), limit cycle fold bifurcation (red line), saddle-stable node bifurcations (solid green line), saddle-unstable node bifurcations (dashed green line), type-1 homoclinic bifurcation (solid brown line), type-2 homoclinic bifurcation (dashed brown line), type-3 homoclinic bifurcation (dashed-dotted brown line), type-4 homoclinic bifurcation (dotted brown line), Bogdanov-Takens bifurcations (BT). The inset zooms into the black square in the figure, showing the homoclinic bifurcations in detail.

the second PDC region is convenient for the purpose of lower power consumption as the steady state current intensity is smaller in this case. It is important, however, to keep in mind the region of bistability where both the stable fixed point and limit cycle coexist. The broader this region is, the more likely bursts of pulses are to occur when the circuit is perturbed, given the hysteretic character of the AH bifurcation. Figure 15 shows the width of the bistability regions in the proximity of both PDC regions versus the resistance, for two values of  $\mu$ . For  $\mu = 0.002 \Omega^{-1}$ , the bistability has a range in the order of 0.001 V at the left side and 0.01 V at the right side. For  $\mu = 0.0002 \Omega^{-1}$ , these widths decrease in two orders of magnitude. In that sense, biasing the circuit in the first PDC region is more convenient. The resistance does not affect the width of the bistability ranges in a substantial way; only for  $R > 10 \Omega$  an increase is observed, although within the same order of magnitude.

It is also of interest to understand how the lethargic time of the excitable spikes with the circuit biased at both the first and second PDC regions is affected by  $\mu$  and  $R$ . An estimation can be provided by computing the period of the stable limit cycle at the value of  $V_0$  corresponding to each AH bifurcation. These calculations are summarized in figure 16. Indeed, for  $\mu \leq 0.002 \Omega^{-1}$ , the period  $T$  is observed to decrease like  $1/\mu$ . This is consistent with the numerical estimation provided by Romeira et al [21],

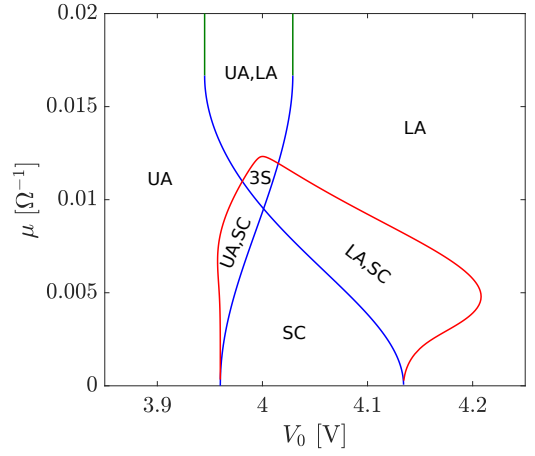


Figure 14. (color online) Stable solutions and the bifurcations that delimit them on the  $(V_0, \mu)$  plane for  $R = 60 \Omega$ . UA: upper attractor point. LA: lower attractor point. SC: stable limit cycle. 3S: coexistence of the three stable solutions.

according to which the period –in actual time units– of stiff, periodic solutions with slow and fast stages is directly proportional to the intrinsic inductance. This in turn implies that the period in normalized time units is inversely proportional to  $\mu$ . Biasing the circuit in the second PDC permits spikes with shorter lethargic times. The resistance has almost no effect on the period; only for  $R = 60 \Omega$  a change is observed (the period decreases in the first PDC and increases in the second PDC, but all in all, it remains in the same order of magnitude for the same value of  $\mu$ ). for  $\mu > 0.002 \Omega^{-1}$ , the decreasing rate of the period relaxes and even reverses in the particular case of  $R = 60 \Omega$ .

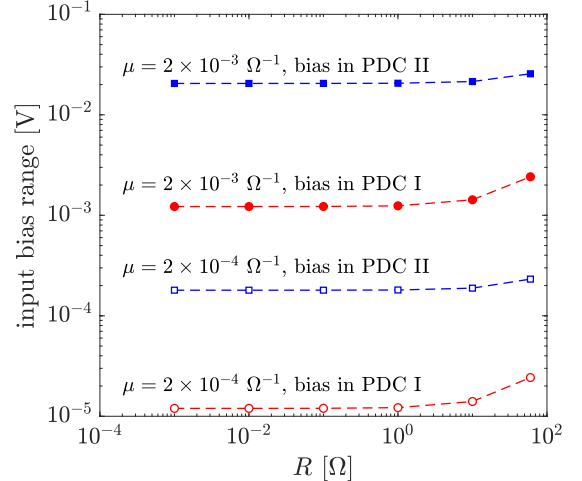


Figure 15. Input bias voltage range of bistability region in terms of the resistance  $R$  at the first and second PDC regions (red circles and blue squares, respectively). The values of the stiffness coefficient are  $\mu = 0.0002 \Omega^{-1}$  (empty symbols) and  $\mu = 0.002 \Omega^{-1}$  (solid symbols).

#### IV. SUMMARY AND CONCLUSIONS

A Liénard-type nonlinear oscillator was proposed to model the dynamics of a double barrier quantum well resonant tunneling diode (DBQW RTD) connected to an electrical DC input. The configurations where the circuit behaves as an excitable spike generator were disclosed in a perspective to design and fabricate optoelectronic, nanoscale devices able of transmission, reception and storage of spike-coded information. The RTD oscillator may exhibit one or more equilibrium solutions in the form of a fixed point or a limit cycle. In particular, the stiffness coefficients determines whether or not the system behaves as a smooth oscillator or a spike generator. Indeed, for a sufficiently small value of  $\mu$ , the periodic solutions exhibit stages of slow and fast dynamics, thus producing an electrical output of periodic spikes.

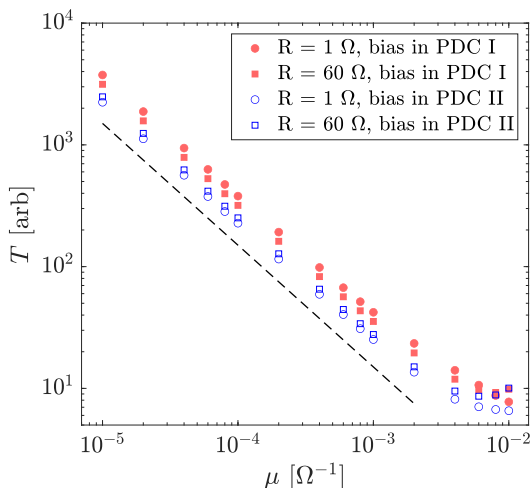


Figure 16. Period of the stable limit cycle versus the stiffness coefficient  $\mu$ , with the circuit biased in the first and second PDC (filled red and empty blue marks, respectively) for resistances  $R = 1 \Omega$  (circles) and  $R = 60 \Omega$  (squares). The dashed line has slope -1 for reference.

When  $V_0$  is tuned in the proximity of the NDC, the equilibrium solution is an attractor point, but perturbations above a certain threshold trigger an excitable response where a single spike – a precursor of the periodic solution – is generated. An electrical input in the form of white noise generates random spikes, including bursts of spikes when the device is biased in the second PDC. These observations are in good agreement with prior experimental results [20, 21]. We identified the reason for the bursting as a bistability range between oscillating be-

havior and rest state. Bifurcation diagrams at fixed low resistances show a stable limit cycle along the NDC region, which folds at both ends, becoming unstable. Both unstable branches coalesce with the fixed point in a subcritical Hopf bifurcation, producing a bias range of bistability at each boundary of the NDC region. A smaller stiffness coefficient implies narrower bias ranges of bistability but a significantly longer period of the limit cycle and subsequent longer lethargic times for excitable responses, thus limiting the speed performance. Biasing the device in the first PDC ensures a narrower bistability range (about one order of magnitude less than in the second PDC) and, consequently, bursts of spikes and hysteretic behavior are less likely. However, this choice has the cost of a higher equilibrium current intensity and, therefore, a higher power consumption.

Significant qualitative changes occur when the resistance surpasses a critical value  $R_C$ , given by the minus reciprocal of the minimal differential conductance at the NDC region (about  $38.5 \Omega$  in for the I-V characteristic chosen in this work). Depending on the input bias voltage, the system may exhibit up to three fixed points, the middle one always being a saddle. In the bifurcation diagram, this is translated as the fixed point branch folding in two saddle-node transitions. The saddle point branch and the unstable ends of the limit cycle branch may coalesce in a homoclinic bifurcation. The device's intrinsic resistance has little effect on the shape of the spikes, the lethargic time and the bias ranges. Nonetheless, a low resistance is preferable for the purpose of low power consumption and to operate under a configuration where the theoretical model is reliable. Experimentally measured I-V characteristics in RTDs are not necessarily smooth curves, or may have more than one NDC [14], and a non-vertical load line may intersect it at several points, which may generate a more complex variety of multistabilities than those observed in this work.

#### ACKNOWLEDGEMENTS

This work was supported in part by the European Commission through the H2020-FET-OPEN Project “ChipAI” under Grant Agreement 82884. We acknowledge fruitful discussions with A. Teruel, R. Prohens and C. Vich regarding the dynamics of slow-fast systems. We thank J. Figueiredo, Universidade de Lisboa, for the fruitful discussion about RTD devices.

[1] Eugene M. Izhikevich. *Dynamical systems in neuroscience : the geometry of excitability and bursting*. Computational neuroscience. MIT Press, Cambridge, Mass.,

London, 2007.

[2] A. L. Hodgkin and A. F. Huxley. A quantitative description of membrane current and its application to con-

- duction and excitation in nerve. *Journal of Physiology*, 117(4):500–544, 1952.
- [3] A. L. Hodgkin, A. F. Huxley, and B. Katz. Measurement of current-voltage relations in the membrane of the giant axon of loligo. *The Journal of physiology*, 116(4):424, 1952.
  - [4] L. Kuhnert, K. I. Agladze, and V. I. Krinsky. Image processing using light-sensitive chemical waves. *Nature*, 337(6204):244–247, 1989.
  - [5] AS Samardak, A Nogaret, NB Janson, A Balanov, I Farrer, and DA Ritchie. Spiking computation and stochastic amplification in a neuron-like semiconductor microstructure. *Journal of Applied Physics*, 109, 2011.
  - [6] D. Goulding, S. P. Hegarty, O. Raskazov, S. Melnik, M. Hartnett, G. Greene, J. G. McInerney, D. Rachinskii, and G. Huyet. Excitability in a quantum dot semiconductor laser with optical injection. *Physical Review Letters*, 98:153903, 2007.
  - [7] F. Selmi, R. Braive, G. Beaudoin, I. Sagnes, R. Kuszelewicz, and S. Barbay. Relative refractory period in an excitable semiconductor laser. *Phys. Rev. Lett.*, 112:183902, May 2014.
  - [8] Sylvain Barbay, Robert Kuszelewicz, and Alejandro M. Yacomotti. Excitability in a semiconductor laser with saturable absorber. *Optics letters*, 36(23):4476–4478, 2011.
  - [9] Paul A. Merolla, John V. Arthur, Rodrigo Alvarez-Icaza, Andrew S. Cassidy, Jun Sawada, Filipp Akopyan, Bryan L. Jackson, Nabil Imam, Chen Guo, Yutaka Nakamura, Bernard Brezzo, Ivan Vo, Steven K. Esser, Rathinakumar Appuswamy, Brian Taba, Arnon Amir, Myron D. Flickner, William P. Risk, Rajit Manohar, and Dharmendra S. Modha. A million spiking-neuron integrated circuit with a scalable communication network and interface. *Science*, 345(6197):668–673, Aug 8 2014.
  - [10] Intel Quark SE Microcontroller. *Intel-SEEIM-4-2016*.
  - [11] J. Zhu, T. Zhang, Y. Yang, and R. Huang. A comprehensive review on emerging artificial neuromorphic devices. *Applied Physics Reviews*, 7(1):11312, 2020.
  - [12] R. Izumi, S. Suzuki, and M. Asada. 1.98 thz resonant-tunneling-diode oscillator with reduced conduction loss by thick antenna electrode. In *2017 42nd International Conference on Infrared, Millimeter, and Terahertz Waves (IRMMW-THz)*, pages 1–2, Aug 2017.
  - [13] Bruno Romeira, José M. L. Figueiredo, and Julien Javaloyes. Delay dynamics of neuromorphic optoelectronic nanoscale resonators: Perspectives and applications. *Chaos: An Interdisciplinary Journal of Nonlinear Science*, 27(11):114323, 2017.
  - [14] J. Wang, K. Alharbi, A. Ofiare, H. Zhou, A. Khalid, D. Cumming, and E. Wasige. High performance resonant tunneling diode oscillators for thz applications. In *2015 IEEE Compound Semiconductor Integrated Circuit Symposium (CSICS)*, pages 1–4, Oct 2015.
  - [15] N. Oshima, K. Hashimoto, D. Horikawa, S. Suzuki, and M. Asada. Wireless data transmission of 30 gbps at a 500-ghz range using resonant-tunneling-diode terahertz oscillator. In *2016 IEEE MTT-S International Microwave Symposium (IMS)*, pages 1–4, May 2016.
  - [16] N. Oshima, K. Hashimoto, S. Suzuki, and M. Asada. Wireless data transmission of 34 gbit/s at a 500-ghz range using resonant-tunneling-diode terahertz oscillator. *Electronics Letters*, 52(22):1897–1898, 2016.
  - [17] S. Diebold, K. Nishio, Y. Nishida, J. . Kim, K. Tsuruda, T. Mukai, M. Fujita, and T. Nagatsuma. High-speed error-free wireless data transmission using a terahertz resonant tunnelling diode transmitter and receiver. *Electronics Letters*, 52(24):1999–2001, 2016.
  - [18] Jue Wang, Abdullah Al-Khalidi, Liquan Wang, Razvan Morariu, Afesomhe Ofiare, and Edward Wasige. 15-gb/s 50-cm wireless link using a high-power compact iii-v 84-ghz transmitter. *IEEE Transactions on Microwave Theory and Techniques*, 66:4698–4705, 2018.
  - [19] M. Hänggi and L. O. Chua. Cellular neural networks based on resonant tunnelling diodes. *International Journal of Circuit Theory and Applications*, 29(5):487–504, 2001.
  - [20] B. Romeira, J. Javaloyes, J. M. L. Figueiredo, C. N. Ironside, H. I. Cantu, and A. E. Kelly. Delayed feedback dynamics of liénard-type resonant tunneling-photo-detector optoelectronic oscillators. *IEEE Journal of Quantum Electronics*, 49(1):31–42, Jan 2013.
  - [21] B. Romeira, J. Javaloyes, C. N. Ironside, J. M. L. Figueiredo, S. Balle, and O. Piro. Excitability and optical pulse generation in semiconductor lasers driven by resonant tunneling diode photo-detectors. *Opt. Express*, 12(8):20931–20940, 2013.
  - [22] B. Romeira, R. Avó, José M. L. Figueiredo, S. Barland, and J. Javaloyes. Regenerative memory in time-delayed neuromorphic photonic resonators. *Scientific Reports*, 6:19510 EP –, Jan 2016. Article.
  - [23] Yu-Chuan Lin, Ram Krishna Ghosh, Rafik Addou, Ning Lu, Sarah M. Eichfeld, Hui Zhu, Ming-Yang Li, Xin Peng, Moon J. Kim, Lain-Jong Li, Robert M. Wallace, Suman Datta, and Joshua A. Robinson. Atomically thin resonant tunnel diodes built from synthetic van der waals heterostructures. *Nature Communications*, 6(1):7311, Jun 2015.
  - [24] A. Mishchenko, J. S. Tu, Y. Cao, R. V. Gorbachev, J. R. Wallbank, M. T. Greenaway, V. E. Morozov, S. V. Morozov, M. J. Zhu, S. L. Wong, F. Withers, C. R. Woods, Y.-J. Kim, K. Watanabe, T. Taniguchi, E. E. Vdovin, O. Makarovskiy, T. M. Fromhold, V. I. Fal’ko, A. K. Geim, L. Eaves, and K. S. Novoselov. Twist-controlled resonant tunnelling in graphene/boron nitride/graphene heterostructures. *Nature Nanotechnology*, 9(10):808–813, Oct 2014.
  - [25] J. N. Schulman, H. J. De Los Santos, and D. H. Chow. Physics-based rtd current-voltage equation. *IEEE Electron Device Letters*, 17(5):220–222, May 1996.
  - [26] Steven H. Strogatz. *Nonlinear Dynamics and Chaos (with applications to Physics, Biology, Chemistry and Engineering)*. CRC Press, 2015.
  - [27] Alfred-Marie Liénard. Etude des oscillations entretenues. *Revue générale de l’électricité*, 23(1):901–912 and 946–954, 1928.
  - [28] B. Lindner, J. Garca-Ojalvo, A. Neiman, and L. Schimansky-Geier. Effects of noise in excitable systems. *Physics Reports*, 392(6):321 – 424, 2004.
  - [29] K. Engelborghs, T. Luzyanina, and D. Roose. Numerical bifurcation analysis of delay differential equations using dde-biftool. *ACM Trans. Math. Softw.*, 28(1):1–21, March 2002.
  - [30] Tetsuya Uemura and P. Mazumder. Design and analysis of resonant-tunneling-diode (rtd) based high performance memory system. *IEICE Trans. Electron*, E82-C(9), 01 1999.